Experiments in Fluids (2025) 66:133
https://doi.org/10.1007/s00348-025-04034-9

RESEARCH ARTICLE

Transition phenomena and intermittency on a Mach 6 flat plate evaluated by three independent flow parameters

Jens Lunte[1] · **Erich Schülein**[1]

Received: 4 December 2024 / Revised: 10 April 2025 / Accepted: 11 April 2025

Abstract

Heat transfer rates, wall pressure and density fluctuations of a flat-plate boundary layer within the laminar–turbulent transition zone were measured at Mach 6 freestream conditions. The combination of the three independent flow parameters enables an extensive insight into the transition phenomena, improves the interpretation of the data and identifies the limitations of the respective measurement techniques. Comparisons between the measurement data culminate in the quantitative description of the transition progress by means of the intermittency distributions, which were calculated from each flow parameter individually. The derived transition locations differ by up to 9.3% in streamwise direction in relation to the average transition Reynolds number.

List of symbols

Greek symbols

γ	Intermittency
ρ	Density

Latin symbols

a, b	Fit variables
f	Frequency
$H_{\Delta x}$	Frequency response of FLDI due to finite focal points spacing
Ind	Indicator function
p	Pressure
r	Radius
R_z	Mean roughness depth
Re_1	Unit Reynolds number
Δs_{opt}	Optical path difference
S	Threshold value of SF
SF	Selection function
St	Stanton number
t	Time
T	Temperature
U	Voltage
u	Streamwise velocity
u_c	Convective velocity of instabilities
x, y, z	Spatial coordinates

Subscript

0	Stagnation conditions
∞	Freestream conditions
lami	Laminar boundary layer condition
turb	Turbulent boundary layer condition

Abbreviations

FLDI	Focused laser differential interferometry
PCB	PCB-132A31 sensors
PDF	Probability density function
PSD	Power spectral density
QIRT	Quantitative infrared thermography

1 Introduction

Adequate prediction of the laminar–turbulent transition on the outer skin of aircraft is complicated by the influence of a large number of parameters that are often neither configurable nor sufficiently documentable in practice (Reshotko 1976). Although the test conditions in wind tunnels can be kept as constant as possible, adequate detection of the local progression of the transition remains a challenge. Quantitatively, the transition progress is commonly described by the scalar intermittency factor γ, which represents the temporal fraction of turbulent flow at a fixed point of the transitional boundary layer and is therefore closely linked to

✉ Jens Lunte
jens.lunte@dlr.de

Erich Schülein
erich.schulein@dlr.de

[1] Department of High Speed Configurations, Institute of Aerodynamics and Flow Technology, DLR, Bunsenstr. 10, 37073 Göttingen, Germany

Published online: 13 June 2025

the formation and migration of turbulent spots (Schneider 2015). Narasimha and Dey (1989) give an overview how the intermittency development in the transitional boundary layer can be modelled, and they indicate several ways to derive the intermittency value from experimental data.

In order to reliably record the distribution of the intermittency in the transition area, for example, the local portion of the turbulent flow must be detected statistically. The criteria for distinguishing between laminar and turbulent states of the boundary layer usually have to be individually adapted to the measurement method and involve the subjective choice of thresholds as well as additional parameters. Another problem is the evaluation of the calculated intermittency values. There is no objective reference value. Often, the determined intermittency is verified by either showing the resilience of the result regarding the subjective choice of thresholds, or by applying different methods to the same data set. But this verification approach neglects the impact of systematic errors in the original raw data on the intermittency result. Schneider (1995) and Veerasamy and Atkin (2020) not only criticised the subjectivity of this practice, but also made suggestions for standardising the procedure in order to improve the comparability of the data.

To evaluate the reliability of alternative methods for intermittency measurements, the present study investigated the transition process on a flat plate using three independent measurement methods to determine the Stanton number distribution, wall pressure fluctuations and density fluctuations. As the flow parameters detect different fluid dynamic aspects of the same laminar–turbulent transition, the comparison of the derived intermittency distributions reveal how consistent the transition location can be determined.

2 Experimental setup

2.1 Wind tunnel facility and model

All experiments were conducted at the Mach 6 flow conditions of the DLR Ludwieg-Tube Facility Göttingen RWG (Schülein 2006; Wagner et al. 2018). The axisymmetric nozzle has an exit diameter of 0.5 m and connects to the closed-type measurement section. A sketch of the facility is shown in Fig. 1a. The storage tube is heated to around 543 K to avoid the condensation of air molecules during the gas expansion in the nozzle and the length of the storage tube allows for run times of up to 330 ms with nearly constant freestream conditions. The measurements comprise a freestream unit Reynolds number Re_1 variation, whose flow characteristics are listed in Table 1. The measured freestream Mach number is 5.98 ± 0.06, and the pitot-pressure fluctuations are around 1.8%, which is a typical value for conventional hypersonic wind tunnel facilities.

To compare the intermittency distributions of three independent measurement techniques, a generic flat plate was chosen as the wind tunnel model. The flat plate, shown

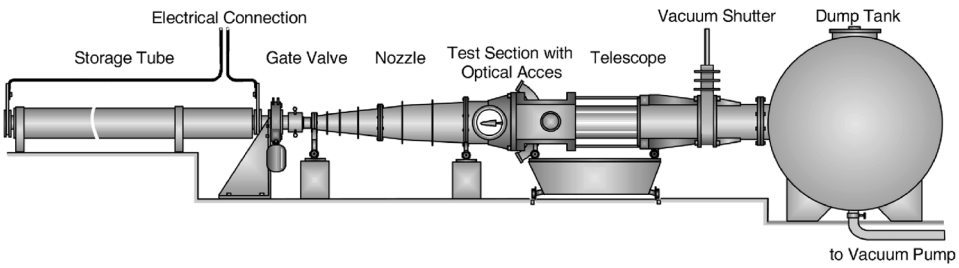

(a) Ludwieg-Tube Facility at DLR Göttingen

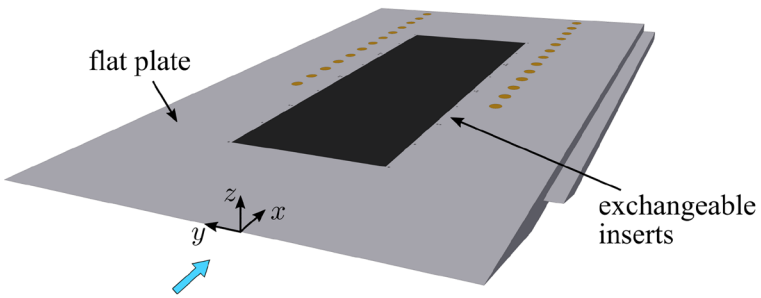

(b) Flat plate model

Fig. 1 Wind tunnel facility and flat-plate model with insert

Table 1 Representative flow parameters at the investigated unit Reynolds numbers at the RWG

Re_1 $[10^6\,\mathrm{m}^{-1}]$	p_0 $[MPa]$	T_0 $[K]$	p_∞ $[Pa]$	T_∞ $[K]$	ρ_∞ $[kg/m^3]$	u_∞ $[m/s]$
8	1.08	543	700	66.6	0.037	978
14	1.89	543	1220	66.6	0.064	978
19	2.55	543	1650	66.6	0.086	978
24	3.32	543	2090	66.6	0.109	978

Table 2 Measurement positions of the PCB sensors at both orientations of the insert plate

Mounting	(x, y) [mm]	
Position	Upstream	Downstream
01	(106.00, −65.00)	(486.00, 65.00)
02	(118.67, −56.33)	(473.33, 56.33)
03	(131.33, −47.67)	(460.67, 47.67)
04	(144.00, −39.00)	(448.00, 39.00)
05	(156.67, −30.33)	(435.33, 30.33)
06	(169.33, −21.67)	(422.67, 21.67)
07	(182.00, −13.00)	(410.00, 13.00)
08	(194.67, − 4.33)	(397.33, 4.33)
09	(207.33, 4.33)	(384.67, − 4.33)
10	(220.00, 13.00)	(372.00, −13.00)
11	(232.67, 21.67)	(359.33, −21.67)
12	(245.33, 30.33)	(346.67, −30.33)
13	(258.00, 39.00)	(334.00, −39.00)
14	(270.67, 47.67)	(321.33, −47.67)
15	(283.33, 56.33)	(308.67, −56.33)
16	(296.00, 65.00)	(296.00, −65.00)

in Fig. 1b, is 400 mm wide, is 669 mm long, and has a leading-edge radius of 0.1 mm. Additionally, the plate has a 150-mm-wide cutout between $x = 96$ mm and $x = 496$ mm for exchangeable inserts to apply various measurement techniques on the same base model.

2.2 Measurement techniques

2.2.1 PCB

The pressure fluctuations inside the boundary layer were measured with PCB-132A31 sensors from the company *PCB Synotech GmbH*, which can evaluate a frequency range from 11 kHz to 1 MHz. A special insert plate, depicted in Fig. 2a, was manufactured to mount a total of 16 sensors diagonally along the spanwise direction to prevent the influence of wake on downstream sensors. The insert was rotated by 180 ° inside the base plate to measure the pressure fluctuations upstream and downstream of the insert centre point in two separate measurement runs. The measurement positions of the PCB sensors are listed in Table 2. The data acquisition was carried out with the A/D-converter modules *TRION-1620-ACC-6-L1B* from *DEWETRON GmbH* at a sampling rate of 2 MHz and 16 bit resolution.

The PCB sensors are known for being susceptible to mechanical vibrations (Willems et al. 2015; Weisberger et al. 2019), so it is important to minimise the transmission of vibrations by using a suitable mounting method (see Schneider 2019 as well as Ort and Dosch 2019). In the current work, the disturbing influence of vibrations was reduced by casting the sensor with its clamp nut in silicone. The assembly is depicted in Fig. 2b. To avoid a direct transmission of the mechanical vibrations, the sensors must not touch the metal, so a small radial gap of 160 µm was kept around each sensor. Although the gap generates additional disturbances inside the boundary layer, the gap was not filled with silicon, because pretests indicated that such small silicon thicknesses attenuate the vibration transmission insufficiently.

Despite the effort, the signal still contains mechanical vibrations at certain frequency ranges, which depend on the specific sensor. To identify the affected frequency ranges, the vibration transmission of the sensors was determined in situ by a mechanical impact (hammer test) on the plate, mounted in the wind tunnel. An example of the recorded power spectral density (PSD) generated by the hammer test is shown in Fig. 3a, where the signal significantly differs from the ideal electric noise floor and distinct peaks are visible. For comparison, the PSD of a laminar boundary layer measured by the identical PCB sensor is shown in Fig. 3b. Although the mechanism for exciting the mechanical vibrations is different between the wind tunnel test and the hammer test, several characteristic peaks from Fig. 3a occur again. Only if the wall pressure fluctuation amplitude exceeds the signal of the electric noise and mechanical vibration at the specific frequency, can the PCB sensor measure the flow physics. To facilitate the interpretation of the data, frequency ranges that are likely to be affected by mechanical vibrations based on the impact test are shown as semitransparent in the PSD plots.

2.2.2 FLDI and QIRT

The other two applied measurement techniques are the focused laser differential interferometry (FLDI) (Lunte and Schülein 2024) for the investigation of density fluctuations inside the boundary layer and the quantitative infrared thermography (QIRT) (Schülein 2014) to determine the heat

Fig. 2 Mounting of the PCB sensors

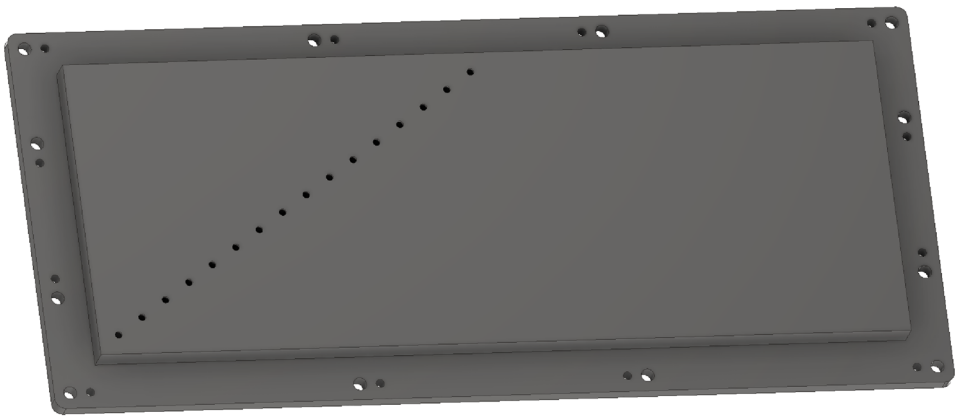

(a) Plate insert with measurement positions of the PCB-sensors

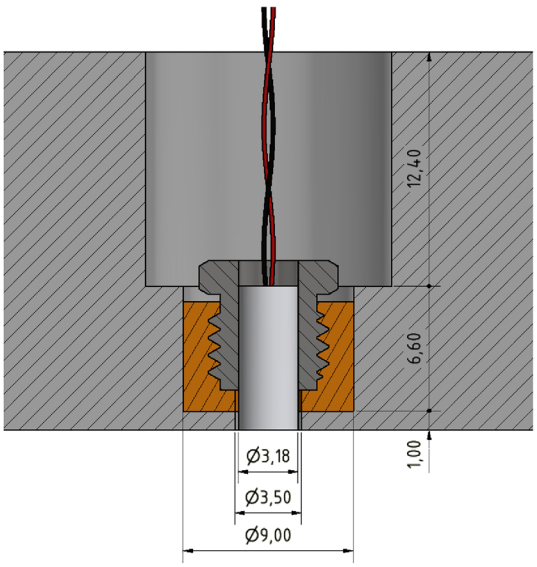

(b) Assembly of the PCB-sensors casted into silicon (depicted in orange)

flux density over the surface. For the sake of brevity and with reference to the given literature for detailed information, only the essential elements of the respective technique are presented.

For the FLDI, an insert with a glass window was manufactured and the laser beam, in contrast to most spanwise applications, was aligned along the wall normal direction. The focal plane was placed inside the boundary layer, and the focus points of the two split partial beams were separated along the streamwise direction by 175 µm, which ensures an upper frequency limit in the MHz range. With the used optical setup, the intensity profiles of the partial beams are completely separated from each other for several millimetres. Thus, the density field of the complete boundary layer and a part of the freestream influence the optical path of each beam in a line integrated way. Density fluctuations lead to optical path differences between the two beams, which were recorded as light intensity variations of the interference signal by a *Thorlabs DET36A2* photodiode. The voltage signals were digitised by a Tektronix DPO 7254 oscilloscope at 25 MHz sampling rate and a theoretical bit resolution of 13.3 bits, utilising the averaging *Hi-Res* mode of the oscilloscope. The FLDI signal was high-pass-filtered at $f = 500$ Hz to reduce the effects of mechanical vibrations caused by the wind tunnel operation on the measurement signal. The FLDI measurements were taken at several positions along the centreline of the insert.

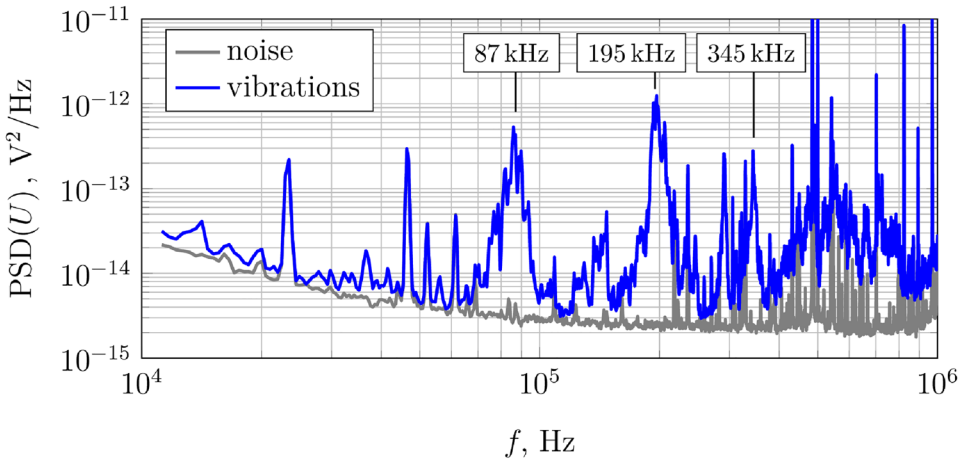

(a) PSD of mechanical vibrations exited by the hammer test

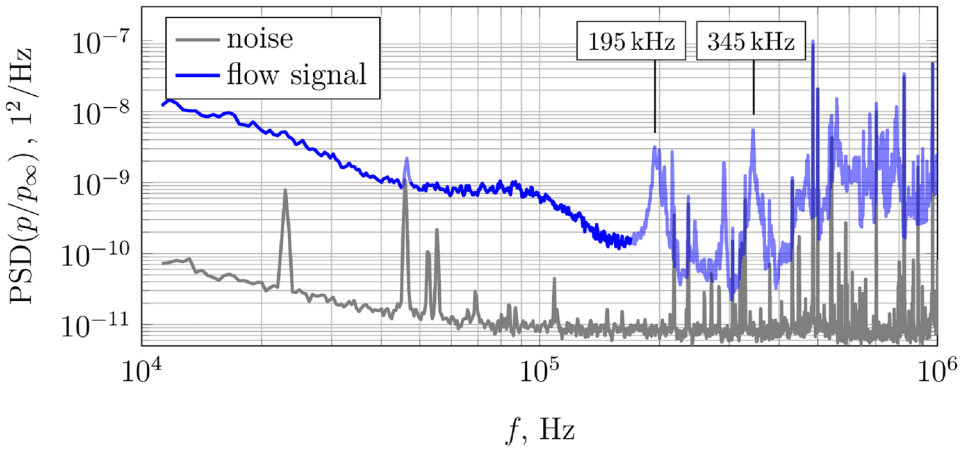

(b) PSD of a laminar boundary layer

Fig. 3 Influence of the mechanical vibrations on the PSD for an exemplary PCB sensor

At QIRT the temporal temperature development of the model surface is recorded through a germanium window in the wind tunnel wall by a *IRCAM EQUUS 327kL* infrared camera at a frame rate of 105 Hz and 100 µs exposure time. For high quality temperature data, a matt black Plexiglas® insert (see Fig. 1b) is mounted due to its high emissivity and low thermal conductivity. The latter reduces the temperature homogenisation in lateral direction as well as in the depths of the material. The Cook and Felderman equation (see Schultz and Jones 1973, Eq. 83) is used to calculate the heat flux density from the temporal wall-temperature development, and with a nondimensionalisation, the Stanton number *St* is obtained as a metric for the heat transfer between model and flow.

3 Results and discussion

3.1 Transition phenomena

Figure 4a presents the surface distribution of the Stanton number generated by the laminar–turbulent transition on a flat plate. As known, the heat fluxes increase significantly during the transition process, but, despite a 2-D model geometry, the *St* values vary along the spanwise direction with an apparent symmetry to the model centreline. Comparable structures were observed in the flat-plate experiments of Willems and Gülhan (2013) (in Fig. 5) and

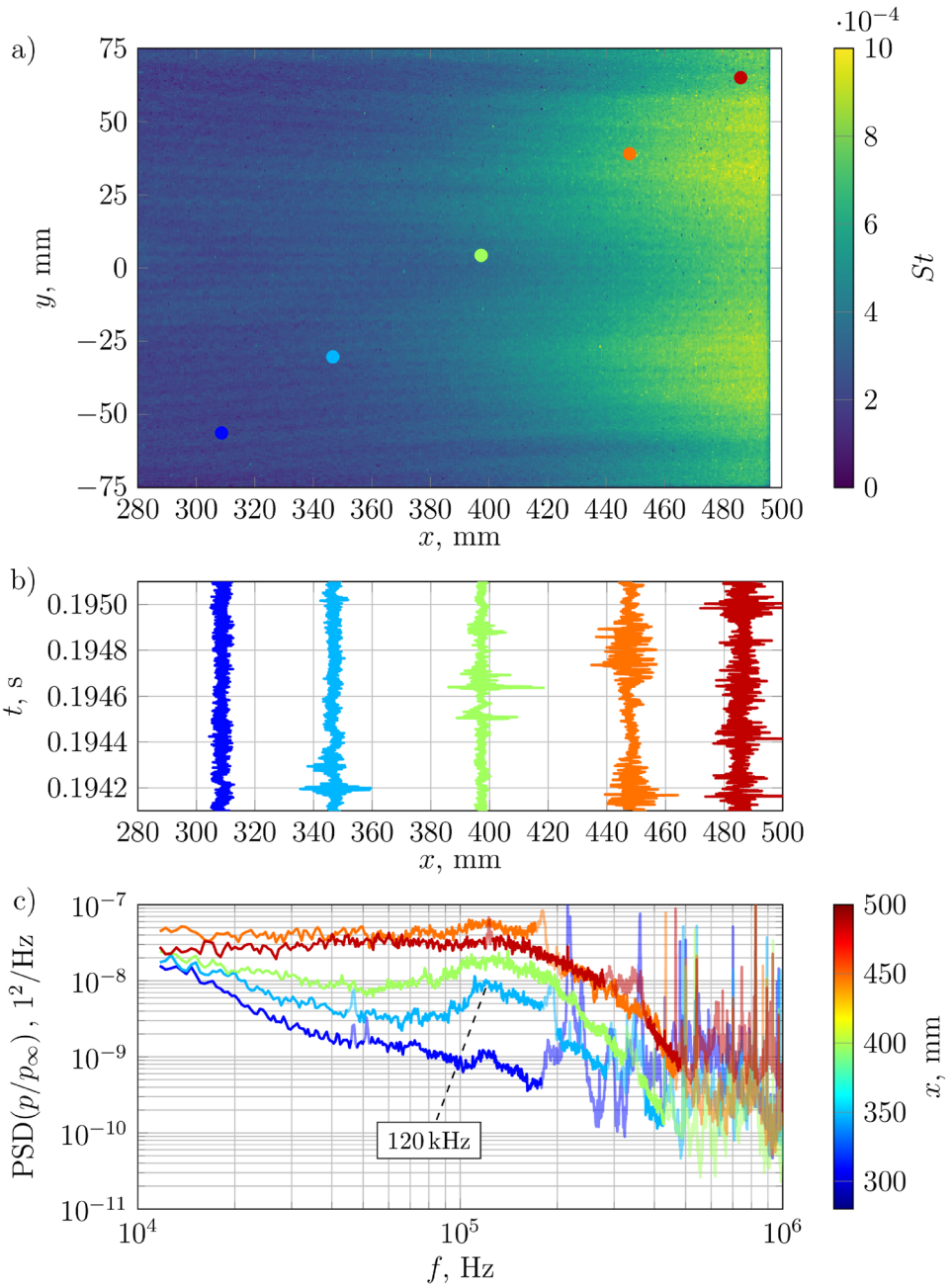

Fig. 4 *St* distributions (**a**), scaled pressure fluctuations (**b**) and PSD of the pressure fluctuations (**c**) on the flat plate

were explained by inconsistent freestream conditions, that depend on the radial distance from the nozzle axis (Willems et al. 2015). A radial dependency of the freestream conditions can occur if the nozzle contour deviates from the ideal shape. Small deviations lead to weak stationary shocks, which excite the instabilities in the boundary layer when they impinge on the plate and cause the observed spanwise varying transition location.

As the spanwise varying transition location must be taken into account when interpreting the PCB data, the measurement position of selected PCB sensors is marked in Fig. 4a by coloured dots. Figure 4b presents the corresponding extracts from the time signal in a scaled manner. Together with the increase in the heat flux due to laminar–turbulent transition, the PCB time traces also change. First, the time signal of the laminar boundary layer is occasionally interrupted by short pulses with increased signal amplitude like at $t = 194.2$ ms in the light blue time trace, which will be identified as the wave package of a second Mack mode instability in the next paragraph. As the transition progresses, the quantity of instabilities increases (green time trace) and finally turbulence spots make up an increasing fraction of the measurement signal (orange and red time trace).

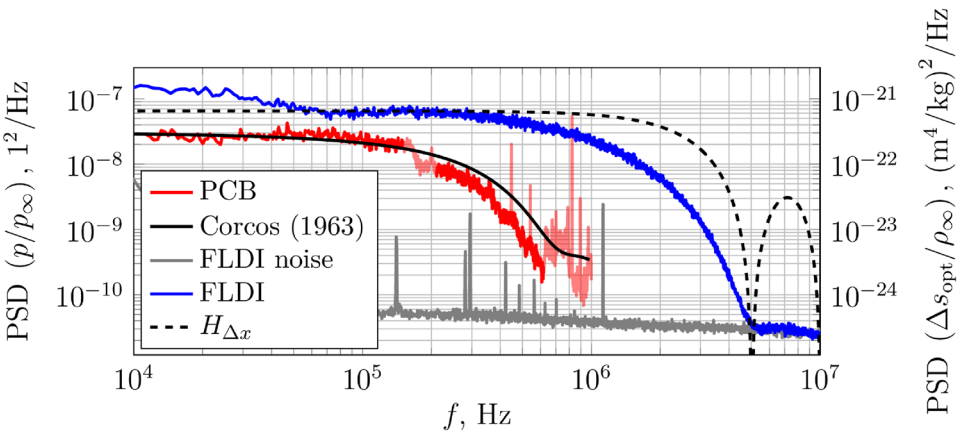

Fig. 5 PSD from PCB and FLDI of a turbulent boundary layer with the estimated amplitude attenuation

The alteration of the power spectral density (PSD) of the pressure fluctuations inside the boundary layer due to the laminar–turbulent transition is displayed in Fig. 4c. The PSD of the most upstream signal (dark blue line) decreases with frequency and shows exemplarily the spectrum of a laminar boundary layer, since no high-frequency fluctuations due to second Mack modes or even turbulence spots exist in the measurement signal. Near the onset of transition (light blue and green curves) a local peak in the PSD emerges at $f \approx 120\,\mathrm{kHz}$. Demetriades (1977) and Stetson et al. (1989) showed that the frequency of the second Mack modes scales inversely proportional with the local boundary layer height and validated a scaling law. The scaling law was used in Lunte and Schülein (2024) to successfully check that the measured peak frequencies on the flat plate correspond to the second Mack modes.

As the transition progresses, the instabilities become more frequent and their amplitude increases until nonlinear effects occur and the instabilities break down to turbulent spots. As the PSD is calculated from a statistical average of individual events, the described transition process leads firstly to a broadening of the second Mack mode peak and finally to a broadband spectrum visible by the orange and red curves.

The PSD of a turbulent boundary layer measured by PCB is compared with a spectra measured by FLDI in Fig. 5, indicating a more broadband frequency spectra in the boundary layer than can be measured by PCB sensors. The amplitude attenuation of PCB sensors is attributed to the spatial size of the sensing element (Beresh et al. 2011), which acts like a low-pass filter for the pressure fluctuations. Corcos (1963) modelled the frequency dependent attenuation below an incompressible turbulent boundary layer based upon the scaled frequency $2\pi fr/u_c$, where r is the radius of the effective sensing area and u_c the convective velocity of the fluctuations. The predicted amplitude response by Corcos (1963) is plotted in Fig. 5 for $u_c = 0.9u_\infty$ (Weisberger et al. 2019) and $r = .7136\,\mathrm{mm}$ (Beresh et al. 2011). Although a theory developed for incompressible flows was applied, the shape of the PSD spectra is matched, which explains the differences to the FLDI data. In addition, the theoretical frequency response $H_{\Delta x}$ of FLDI due to the finite distance between the two focal points was calculated (Lunte and Schülein 2024) and added to Fig. 5 to indicate that, despite the higher frequency bandwidth of FLDI, the spectrum of the turbulent boundary layer is measured attenuated.

3.2 Determination of the intermittency

The progress of the laminar–turbulent transition is quantified by the intermittency value, which represents the temporal fraction the boundary layer is turbulent at any point and therefore is applied in the final phase of the transition process, where turbulent spots intermittently traverse along the boundary layer. Over the decades, many methods for determining the intermittency value have been published, which are often based on the same proven procedure (Veerasamy and Atkin 2020). The most important element of each method is defining a selection function SF that is sensitive to turbulent spots and can handle the intrinsic measurement errors of the data set. For measured flow properties whose static value and fluctuation amplitude change in the turbulent case (e.g. heat flux), a simple selection function like a moving root mean square calculation can be sufficient for the reliable detection of turbulent spots. If the static value of the measured variable remains unaltered, the appropriate choice of a selection function is much more challenging. In the following, a selection function is outlined with which turbulence spots can be detected from the measured pressure fluctuations as shown in Fig. 6a. The selection function utilises the increased amplitude and the more broadband frequency spectrum of the pressure fluctuations in the turbulent case and is based on the wavelet transformation (Torrence and Compo 1998), which can be seen in Fig. 6b. For the current analysis, a Morlet wavelet with a nondimensional frequency of 4π was chosen, as it resembles the wave packet

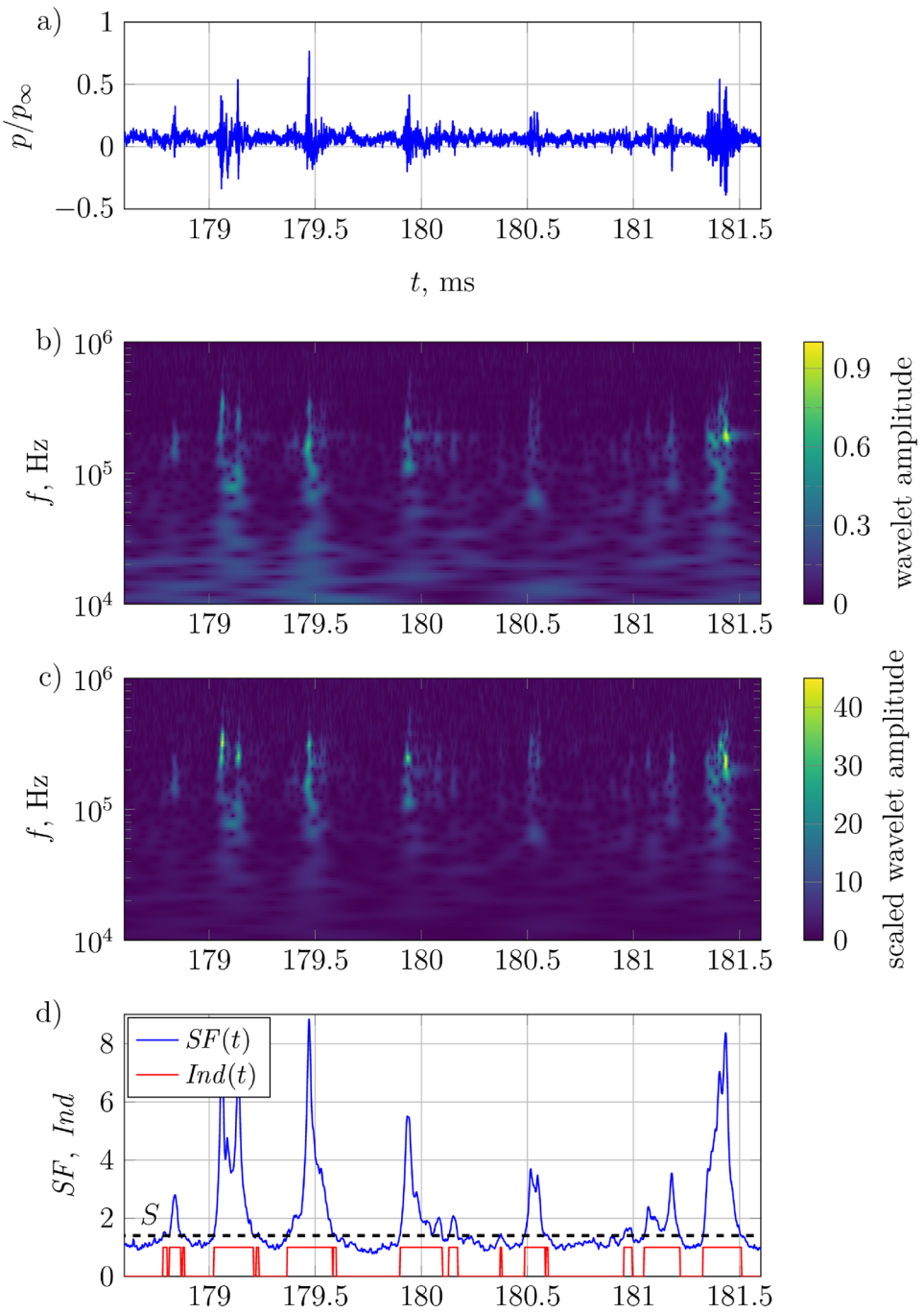

Fig. 6 Steps of the intermittency determination method. The time signal (**a**), corresponding wavelet transformation (**b**) and scaled wavelet transformation (**c**) by the spectra of a laminar boundary layer visualise the data preparation. The selection function SF, the threshold S and the indicator function Ind (**d**) show the classification process of the boundary layer

of a second Mack mode (see Fig. 12 in Lunte and Schülein 2024). Each decade of the frequency bandwidth was discretised by fifty frequencies.

The computer-aided detection of turbulence spots is hampered by noise signals; hence, Schneider (1995) recommends scaling the measurement data with the signal from the laminar boundary layer, whereby intrinsic disturbances of the measurement technology such as electronic noise or vibrations are attenuated. To implement this concept, laminar sections of the wavelet transformations were extracted by hand and averaged to get a statistically representative wavelet frequency spectrum of a laminar boundary layer, which were used to calculate a scaled wavelet spectrum (see Fig. 6c). The correct selection of laminar segments can be checked, since the scaled laminar boundary layer is by definition one, so the probability density function (PDF) of SF should also have a peak at one (see Fig. 7). Measurement positions, where the progress of the transition did not allow the extraction of laminar segments,

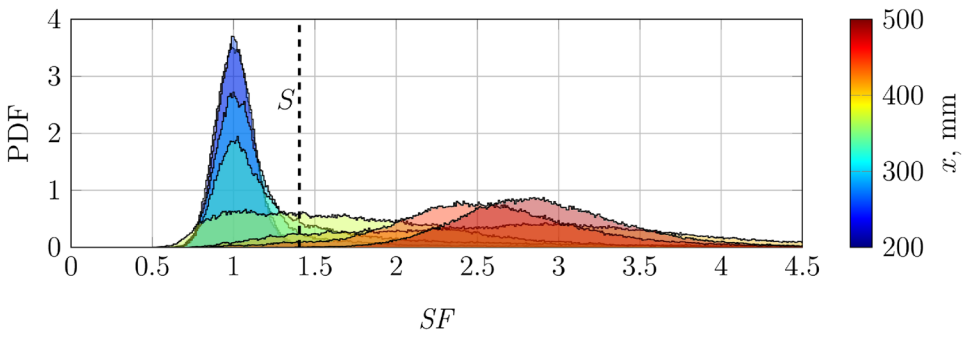

Fig. 7 The probability density functions of *SF* at various streamwise positions undergo a shift to higher *SF* values due to the ongoing transition process

the representative laminar wavelet spectrum was reused from the measurement position immediately upstream.

The selection function *SF* now averages all scaled wavelet frequencies for each point in time and shows in Fig. 6d the desired high sensitivity regarding turbulent spots and values close to one for the laminar sections. A threshold is used to classify the boundary layer flow as either laminar or turbulent, which is visualised by the indicator function *Ind* in Fig. 6d. The statistical average of *Ind* yields the intermittency γ. The threshold value S is selected as recommended by Veerasamy and Atkin (2020) and is based on the measurement position immediately upstream of the transition onset. The threshold was chosen by the 1 ‰-quantile of a fitted log-normal distribution through the laminar probability density function. The selected threshold means that for a laminar boundary layer 1 ‰ of the data points are erroneously classified as turbulent, which is deemed tolerable in terms of the overall accuracy. As the same threshold value is used at all measurement positions for the respective freestream condition, the comparability between the measurement positions is preserved.

The same procedure for calculating the intermittency values was applied to the published focused laser differential interferometry (FLDI) data (Lunte and Schülein 2024), which was measured on the same flat-plate model, and complements the comparison.

Intermittency based on QIRT results: For the time-averaged QIRT results, an individual detection of turbulent spots is conceptually not possible. But the measured mean Stanton number can be interpreted as the local average between the heat transfer rate of the laminar (St_{lami}) and turbulent (St_{turb}) boundary layer weighted by the intermittency factor (Dhawan and Narasimha 1958; Narasimha 1985):

$$\begin{aligned} St &= (1-\gamma)\cdot St_{\mathrm{lami}} + \gamma \cdot St_{\mathrm{turb}} \\ \Leftrightarrow\ \gamma &= \frac{St - St_{\mathrm{lami}}}{St_{\mathrm{turb}} - St_{\mathrm{lami}}} \end{aligned} \tag{1}$$

For the intermittency comparison in this work, the local St_{lami} and St_{turb} are described by power functions $St = a \cdot Re_x^b$ based on the respective heat loads at the transition onset

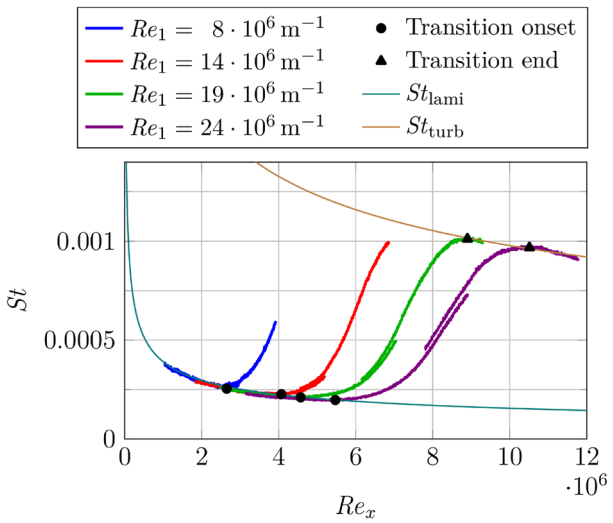

Fig. 8 Spanwise averaged *St* distributions and derived data for determining the intermittency

and end for the investigated Re_1 variation. Figure 8 shows the development of the spanwise averaged ($|y| \leq 25$ mm) *St* during the laminar–turbulent transition for the individual Re_1. Although the averaging of the spanwise inhomogeneous transition onset (see Fig. 4a) makes the derived transition zone appear longer by some extent, the averaging was necessary to calculate a representative intermittency distribution. Due to the limited field of view, the heat flux distribution for each Re_1 was recorded in two spatial segments. The observable transition delay at higher Re_1 is a known effect in conventional hypersonic wind tunnels, which is attributed to a reduction of the freestream noise level and which is already modelled heuristically by Ross (1972). In the literature (Brinich 1956; Benard et al. 2006), the onset and end of transition are commonly identified by the local minimum and maximum of the *St* curve. The determined positions are marked in Fig. 8 and used to fit the curves St_{lami} and St_{turb}. As only two data points are available for the transition end, the exponent was set to $b = -1/3$ based on the results of Lunte and Schülein (2019). The curve progression for St_{lami} and St_{turb} is shown in Fig. 8, and the relevant values are

Table 3 Extracted locations for the transition onset and end as well as the regression results

Re_1 $\left[10^6\ \mathrm{m}^{-1}\right]$	Transition onset (Re_x, St)	Transition end (Re_x, St)
8	$(2.65 \cdot 10^6, 2.54 \cdot 10^{-4})$	$(-, -)$
14	$(4.07 \cdot 10^6, 2.27 \cdot 10^{-4})$	$(-, -)$
19	$(4.57 \cdot 10^6, 2.10 \cdot 10^{-4})$	$(8.90 \cdot 10^6, 10.11 \cdot 10^{-4})$
24	$(5.47 \cdot 10^6, 1.97 \cdot 10^{-4})$	$(10.51 \cdot 10^6, 9.67 \cdot 10^{-4})$
(a, b)	$(0.099, -0.400)$	$(0.211, -1/3)$

summarised in Table 3. With this approximation for St_{lami} and St_{turb} the intermittency value can be calculated using equation (1). According to definition, γ is set to 0 upstream of the transition onset and set to 1 downstream of the transition end.

3.3 Intermittency distribution along the plate

The calculated intermittency distributions based on the heat transfer, pressure and density fluctuations are presented in Fig. 9 for each investigated Re_1. At first glance, all flow parameters provide plausible and mutually consistent intermittency results. But with PCB sensors, the intermittency values are more erratic, which can be ascribed to the diagonal measuring positions of the PCB sensors in conjunction with the already discussed spanwise variation of the transition location. Additionally the PCB sensors detect the transition location furthest upstream, which may be attributed to the invasive measurement method. For the sensors, holes had to be drilled in the insert plate and, due to the vibration decoupling, a 160-µm-wide cavity remains around the individual sensors (see Fig. 2b). The additional interference caused by these gaps can directly influence the measurable transition location.

Another hypothesis is that the intermittency distributions, derived from unsteady quantities (PCB and FLDI), should lead the intermittency values of mean quantities (QIRT), because the latter requires a significant mean flow distortion. In this case, the FLDI results lag behind the intermittency values from PCB. In this context, consider that PCB measures the pressure fluctuations at the wall and FLDI measures the density fluctuations integrated through the complete boundary layer. It might be possible that the pressure fluctuation field of turbulent spots can be detected earlier at the wall than the density fluctuations inside the boundary layer. While it was pointed out in Lunte and Schülein (2024) that the detection of weak density fluctuations, like second Mack modes, is hampered in the wall normal FLDI configuration, the density amplitude of turbulent spots stick out clearly from the freestream noise. To check whether the weak pressure fluctuations of the second Mack modes in the PCB data cause the upstream shift in the intermittency distribution,

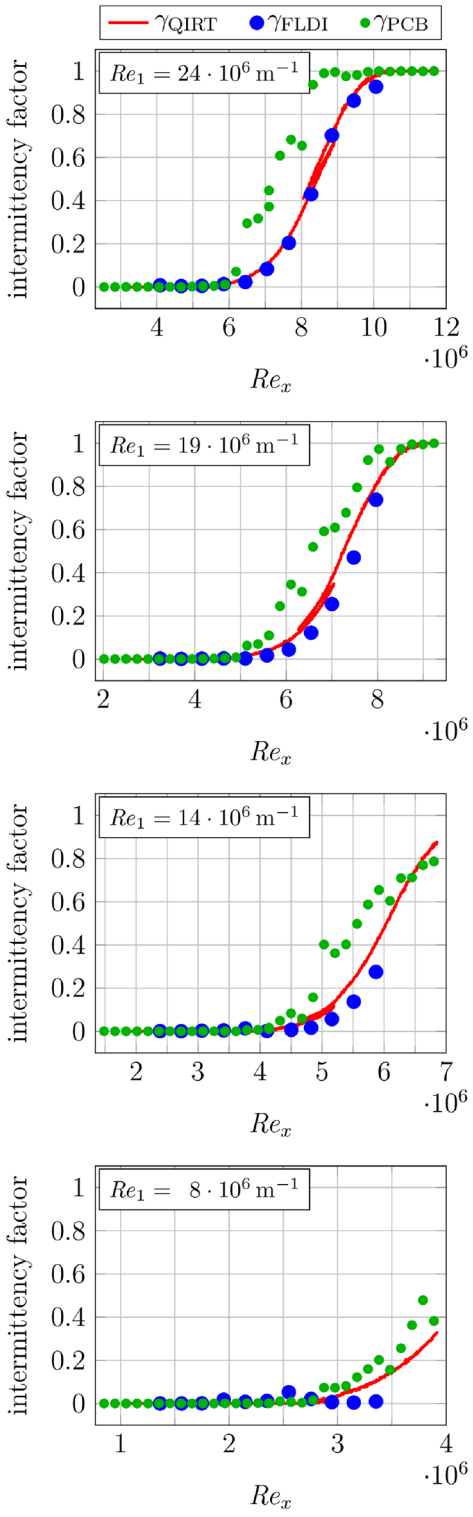

Fig. 9 Comparison of the determined intermittency distributions based on different methods and flow variables for four investigated Re_1 in the transitional boundary layer of a flat plate

a re-evaluation of the intermittency was performed with band-stop filtered PCB data between $f = 80$ to 220 kHz. This frequency band exclusion had only a minor impact on the intermittency results, which means that the evaluation algorithm primarily detects turbulent spots as intended and false detections of second Mack modes are not the reason for the upstream shift of the intermittency for PCB.

If the intermittency results of QIRT and FLDI are compared with each other, there is excellent agreement at $Re_1 = 24e6\,\mathrm{m}^{-1}$. For the smaller Re_1 the agreement decreases and according to the FLDI data the transition position is further downstream. For the two most downstream measurement positions of γ_{FLDI} at $Re_1 = 8e6\,\mathrm{m}^{-1}$ the underlying time signals were visually cross-checked for turbulent spots. Although isolated turbulent spots were observed, their temporal share of the total measurement time was low, so that an intermittency value close to zero is plausible for the positions checked and the deviation from the other methods is unlikely due to a faulty evaluation algorithm.

One explanation for the differences between the measurement techniques may lie in the use of the respective optimised insert plates. The insert plates are manufactured from different materials and the different surface temperature rise during the measurement period can influence the transition location. Also, the surface roughness of each insert was evaluated by measuring the mean roughness depth R_z, which was below 1.5 µm for all inserts and is assessed as uncritical in relation to the present boundary layer thickness. In addition, each time the insert plate was changed, the interface between the base plate and the insert had to be realigned flush and these different boundary conditions may cause a fluid mechanical shift in the transition location.

To quantitatively compare the specific transition locations between the three measurement techniques, the plate position with 50% intermittency is listed in Table 4. Although the structurally identical transition was examined with all techniques, the measured transition position differs by several centimetres. These discrepancies illustrate the caution with which experimental intermittency distributions must be handled, as unintended manipulation of the natural transition by the experimental implementation cannot be ruled out. Another aspect concerns whether all three flow quantities should predict the identical transition position at all.

Table 4 Streamwise position where 50% intermittency is reached

	50% intermittency position [mm]		
$Re_1[10^6\,\mathrm{m}^{-1}]$	QIRT	PCB	FLDI
8	–	–	–
14	431	397	–
19	382	346	396
24	348	303	351

Although statistically the same state of the boundary layer was investigated, each data set represents a separate transition criterion, which may well lead to a different detection result.

Past studies (Potter and Whitfield 1962; Pate 1978) have also compared how consistently the transition location can be determined with different measurement methods. Even then, the quantitative transition location varied significantly between the different methods and showed systematic shifts. If transition data sets are compiled from various sources, such systematic deviations impede the formulation of correlation laws and their applicability. To improve accuracy, the transition results of the individual methods were correlated with one another back then. The results from Fig. 9 and Table 3 as well as 4 make a scientific contribution to this approach by comparing modern methods.

4 Conclusion

The natural laminar–turbulent transition on a flat plate at Mach 6 was investigated sequentially using three independent methods for intermittency detection based on distributions of mean Stanton number, unsteady wall pressure fluctuations and density fluctuations in the boundary layer. The investigation of the measurement data revealed the expected fluid mechanical phenomena of a transitional boundary layer like second Mack modes and turbulent spots with their respective effect on the PSD and time-averaged heat transfer rates. The comparison of the independent flow quantities revealed the limitations of the respective measurement technique and demonstrated the invaluable benefit of having multiple perspectives on the same flow phenomenon for correctly interpreting the measurement data. So, the spanwise variation of the transition position, revealed by the *St* distributions, had to be considered in the analysis of the PCB data. Also, the upper frequency limits of the PCB sensors as well as FLDI are insufficient to measure the complete frequency bandwidth of the turbulent boundary layer without attenuation.

To quantitatively describe the progress of the laminar–turbulent transition, the intermittency distribution was calculated from all three flow quantities. The measurements of the pressure and density fluctuations necessitated the development of a selection function that is sensitive to the passage of turbulent spots to reliable classify the boundary layer as either laminar or turbulent based on a threshold. The selection function utilised the higher fluctuation amplitude and more broadband frequency spectra of a turbulent boundary layer. The comparison of the intermittency results revealed that the location of 50% intermittency differed between the three techniques by up to 9.3% in relation to the average transition Reynolds number. This discrepancy might have its

origin in the experimental implementation, but it illustrates how critical results of a single measurement technique must be considered despite careful execution.

Acknowledgements This work was supported by Basic Funding from the German MoD (BMVg). The authors are grateful for the technical and experimental assistance from the RWG staff.

Author Contributions All authors contributed equally to this work.

Funding Open Access funding enabled and organized by Projekt DEAL.

Data Availability No data sets were generated or analysed during the current study.

Declarations

Conflict of interest The authors declare no conflict of interest.

References

Benard E, Cooper RK, Sidorenko A (2006) Transitional and turbulent heat transfer of swept cylinder attachment line in hypersonic flow. Int J Heat Mass Transf 49(5–6):836–843. https://doi.org/10.1016/j.ijheatmasstransfer.2005.10.006

Beresh SJ, Henfling JF, Spillers RW, Pruett BOM (2011) Fluctuating wall pressures measured beneath a supersonic turbulent boundary layer. Phys Fluids 10(1063/1):3609271

Brinich PF (1956) Effects of leading-edge geometry on boundary layer transition at Mach 3.1. Technical report, NACA TN 3659

Corcos GM (1963) Resolution of pressure in turbulence. J Acoust Soc Am 35(2):192–199. https://doi.org/10.1121/1.1918431

Demetriades A (1977) Laminar boundary layer stability measurements at Mach 7 including wall temperature effects. Technical report, Ford Aerospace and Communications Corp (AFOSR-TR-77-1311)

Dhawan S, Narasimha R (1958) Some properties of boundary layer flow during the transition from laminar to turbulent motion. J Fluid Mech 3(4):418–436. https://doi.org/10.1017/S0022112058000094

Lunte J, Schülein E (2019) Heat transfer amplifications in transitional shock-wave/boundary-layer interactions. AIAA 2019-3440, AIAA Aviation 2019 Forum. https://doi.org/10.2514/6.2019-3440

Lunte J, Schülein E (2024) Wall-normal focused laser differential interferometry. AIAA J 62(4):1366–1374. https://doi.org/10.2514/1.j063258

Narasimha R (1985) The laminar–turbulent transition zone in the boundary layer. Prog Aerosp Sci 22(1):29–80. https://doi.org/10.1016/0376-0421(85)90004-1

Narasimha R, Dey J (1989) Transition-zone models for 2-dimensional boundary layers: a review. Sadhana 14:93–120. https://doi.org/10.1007/BF02812002

Ort D, Dosch JJ (2019) Influence of mounting on the accuracy of piezoelectric pressure measurements for hypersonic boundary layer transition. AIAA 2019-2292, AIAA Scitech 2019 Forum. https://doi.org/10.2514/6.2019-2292

Pate SR (1978) Dominance of radiated aerodynamic noise on boundary-layer transition in supersonic-hypersonic wind tunnels. Theory and application. Technical report, Arnold Engineering Development Center AEDC-TR-77-107

Potter JL, Whitfield JD (1962) Effects of slight nose bluntness and roughness on boundary-layer transition in supersonic flows. J Fluid Mech 12(4):501–535. https://doi.org/10.1017/S0022112062000385

Reshotko E (1976) Boundary-layer stability and transition. Annu Rev Fluid Mech 8:311–349. https://doi.org/10.1146/annurev.fl.08.010176.001523

Ross R (1972) A simple formula for flat plate boundary-layer transition in supersonic wind tunnels. AIAA J 10(3):336–337. https://doi.org/10.2514/3.6585

Schneider SP (1995) Improved methods for measuring laminar-turbulent intermittency in boundary layers. Exp Fluids 18:370–375. https://doi.org/10.1007/BF00211394

Schneider SP (2015) Developing mechanism-based methods for estimating hypersonic boundary-layer transition in flight: the role of quiet tunnels. Prog Aerosp Sci 72:17–29. https://doi.org/10.1016/j.paerosci.2014.09.008

Schneider SP (2019) Towards a process for calibrating 1-MHz pressure-fluctuation sensors with small pressure steps in a shock tube. Final Report for AFOSR Grant FA9550-16-1-0407, AFRL-AFOSR-VA-TR-2019-0362

Schülein E (2006) Skin friction and heat flux measurements in shock/boundary layer interaction flows. AIAA J 44(8):1732–1741. https://doi.org/10.2514/1.15110

Schülein E (2014) Effects of laminar-turbulent transition on the shock-wave/boundary-layer interaction. In: AIAA 2014-3332, 44th AIAA fluid dynamics conference. https://doi.org/10.2514/6.2014-3332

Schultz DL, Jones TV (1973) Heat-transfer measurements in short-duration hypersonic facilities. AGARDograph No. 165

Stetson KF, Thompson ER, Donaldson JC, Siler LG (1989) Laminar boundary layer stability experiments on a cone at Mach 8, part 5 - tests with a cooled model. In: AIAA 1989-1895, 20th Fluid dynamics, plasma dynamics and lasers conference. https://doi.org/10.2514/6.1989-1895

Torrence C, Compo GP (1998) A practical guide to wavelet analysis. Bull Am Meteorol Soc 79(1):61–78

Veerasamy D, Atkin C (2020) A rational method for determining intermittency in the transitional boundary layer. Exp Fluids. https://doi.org/10.1007/s00348-019-2856-5

Wagner A, Schülein E, Petervari R, Hannemann K, Ali S, Cerminara A, Sandham ND (2018) Combined free-stream disturbance measurements and receptivity studies in hypersonic wind tunnels by means of a slender wedge probe and direct numerical simulation. J Fluid Mech 842:495–531. https://doi.org/10.1017/jfm.2018.132

Weisberger JM, Bathel BF, Herring GC, King RA, Chou A, Jones SB (2019) Two-point focused laser differential interferometry second-mode measurements at Mach 6. AIAA 2019-2903, AIAA Aviation 2019 Forum. https://doi.org/10.2514/6.2019-2903

Willems S, Gülhan A (2013) Experiments on shock induced laminar-turbulent transition on a flat plate at Mach 6. In: 5th European conference for aeronautics and space sciences (EUCASS)

Willems S, Gülhan A, Steelant J (2015) Experiments on the effect of laminar-turbulent transition on the SWBLI in H2K at Mach 6. Exp Fluids. https://doi.org/10.1007/s00348-015-1904-z